ARTICLES
https://doi.org/10.1038/s41558-021-01139-x

nature climate change



# Enhanced North Pacific impact on El Niño/Southern Oscillation under greenhouse warming

Fan Jia[1], Wenju Cai[2,3]✉, Bolan Gan[3,4], Lixin Wu[3]✉ and Emanuele Di Lorenzo[5]

**A majority of El Niño/Southern Oscillation (ENSO) events are preceded by the North Pacific Meridional Mode (NPMM), a dominant coupled ocean–atmospheric mode of variability. How the precursory NPMM forcing on ENSO responds to greenhouse warming remains unknown. Here, using climate model ensembles under high-emissions warming scenarios, we find an enhanced future impact on ENSO by the NPMM. This is manifested by increased sensitivity of boreal-winter equatorial Pacific winds and sea surface temperature (SST) anomalies to the NPMM three seasons before. The enhanced NPMM impact translates into an increased frequency of NPMM that leads to an extreme El Niño or La Niña. Under greenhouse warming, higher background SSTs cause a nonlinear evaporation–SST relationship to more effectively induce surface wind anomalies in the equatorial western Pacific, conducive to ENSO development. Thus, NPMM contributes to an increased frequency of future extreme ENSO events and becomes a more influential precursor for their predictability.**

El Niño/Southern Oscillation (ENSO), alternating between its warm phase El Niño and cold phase La Niña, is a consequential mode of climate variability affecting extreme weather, agriculture and ecosystems worldwide[1,2]. Since 1950, a majority of the El Niño and La Niña events were preceded by sea surface temperature (SST) anomalies associated with the North Pacific Meridional Mode (NPMM), a dominant mode of coupled ocean–atmosphere variability in the North Pacific[3,4] (Supplementary Fig. 1). The NPMM is initiated mainly by a pattern of North Pacific atmospheric variability[3,5–7]. Specifically, when negative sea level pressure anomalies over the central subtropical North Pacific (15° N–45° N, 150° E–120° W) in boreal winter weaken the northeast trade winds over the subtropical eastern Pacific, the associated decrease in wind speed reduces the evaporative heat loss, leaving a warm SST anomaly 'footprint'[5,8] in the underlying ocean. The warm SST anomalies extend southwestwards to the Equator via a wind–evaporation–SST (WES) feedback[9,10], forming a distinct positive NPMM pattern peaking in boreal spring (Supplementary Fig. 1a). The pattern features a covarying meridional north-minus-south positive SST gradient and tropical surface westerly wind anomalies, which is conducive to ENSO that matures in the ensuing boreal winter.

ENSO events preceded by the NPMM include the 1982, 1997 and 2015 extreme El Niño events and the 1998 extreme La Niña event (Supplementary Fig. 1b), which caused extreme weather events worldwide and billions of dollars in damage[1,2]. Model simulations reveal a similar relationship, with a significant positive correlation between the NPMM index in boreal spring and ENSO index in the ensuing winter[11–14]. In particular, positive NPMM events show some skill at predicting El Niño events[12,15], and if information of the associated subtropical winds is incorporated in prediction models, the ENSO prediction skill is increased[16,17]. Coupled with ENSO SST anomalies[10], the NPMM is suggested to favour generation of central Pacific (CP) ENSO[7,18,19], a type of event that has the largest SST anomalies in the tropical central Pacific[20–22], although all extreme El Niño events since 1950 were preceded by a positive NPMM[11–14]. A decadal strengthening of the NPMM is also found to increase ENSO complexity[23,24] and partly explain an ENSO property shift from an eastern Pacific type to a CP type around 1999/2000[25–27], contributing to the consensus that the NPMM is an influential trigger of tropical Pacific variability on various timescales[28–36]. Together with initial equatorial subsurface conditions[28] and variability from the South Pacific[29–33], the NPMM contributes to ENSO generation and ENSO diversity.

However, how the NPMM forcing on ENSO responds to greenhouse warming is an important issue but remains unknown. Using outputs from the fifth and sixth phases of the Coupled Model Intercomparison Project (CMIP5 and CMIP6), in this article we show an enhanced impact of the NPMM on ENSO under greenhouse warming.

## Forcing of ENSO by the NPMM and model selections

To depict the NPMM mode, we apply a maximum covariance analysis (MCA) on quadratically detrended monthly SST and surface wind anomalies over the Pacific Ocean[3] in observations and modelling outputs (see Observed and CMIP5/6 data in Methods). Concurrent ENSO-related SST and wind variability are removed by linear regressions of SST and wind anomalies onto the monthly cold tongue index (CTI, that is, SST anomalies averaged in the region of 6° S–6° N, 180°–90° W) before the MCA analysis[3,13,15,31–33]. The SST expansion coefficient of MCA scaled to have a standard deviation (s.d.) of 1.0 is taken to describe the temporal variations of the NPMM, hereafter referred to as an NPMM–SST index. Linear regression of SST and surface wind anomalies onto the NPMM–SST index is taken to represent the spatial pattern of the NPMM (see Depiction of the NPMM in Methods).

[1]CAS Key Laboratory of Ocean Circulation and Waves, Institute of Oceanology/Center for Ocean Mega-Science, Chinese Academy of Sciences and Pilot National Laboratory for Marine Science and Technology (Qingdao), Qingdao, China. [2]Centre for Southern Hemisphere Oceans Research (CSHOR), CSIRO Oceans and Atmosphere, Hobart, Tasmania, Australia. [3]Key Laboratory of Physical Oceanography and Frontiers Science Center for Deep Ocean Multispheres and Earth System, Ocean University of China and Pilot National Laboratory for Marine Science and Technology (Qingdao), Qingdao, China. [4]International Laboratory for High-Resolution Earth System Prediction, Texas A&M University, College Station, TX, USA. [5]School of Earth and Atmospheric Sciences, Georgia Institute of Technology, Atlanta, GA, USA. ✉e-mail: Wenju.Cai@csiro.au; lxwu@ouc.edu.cn

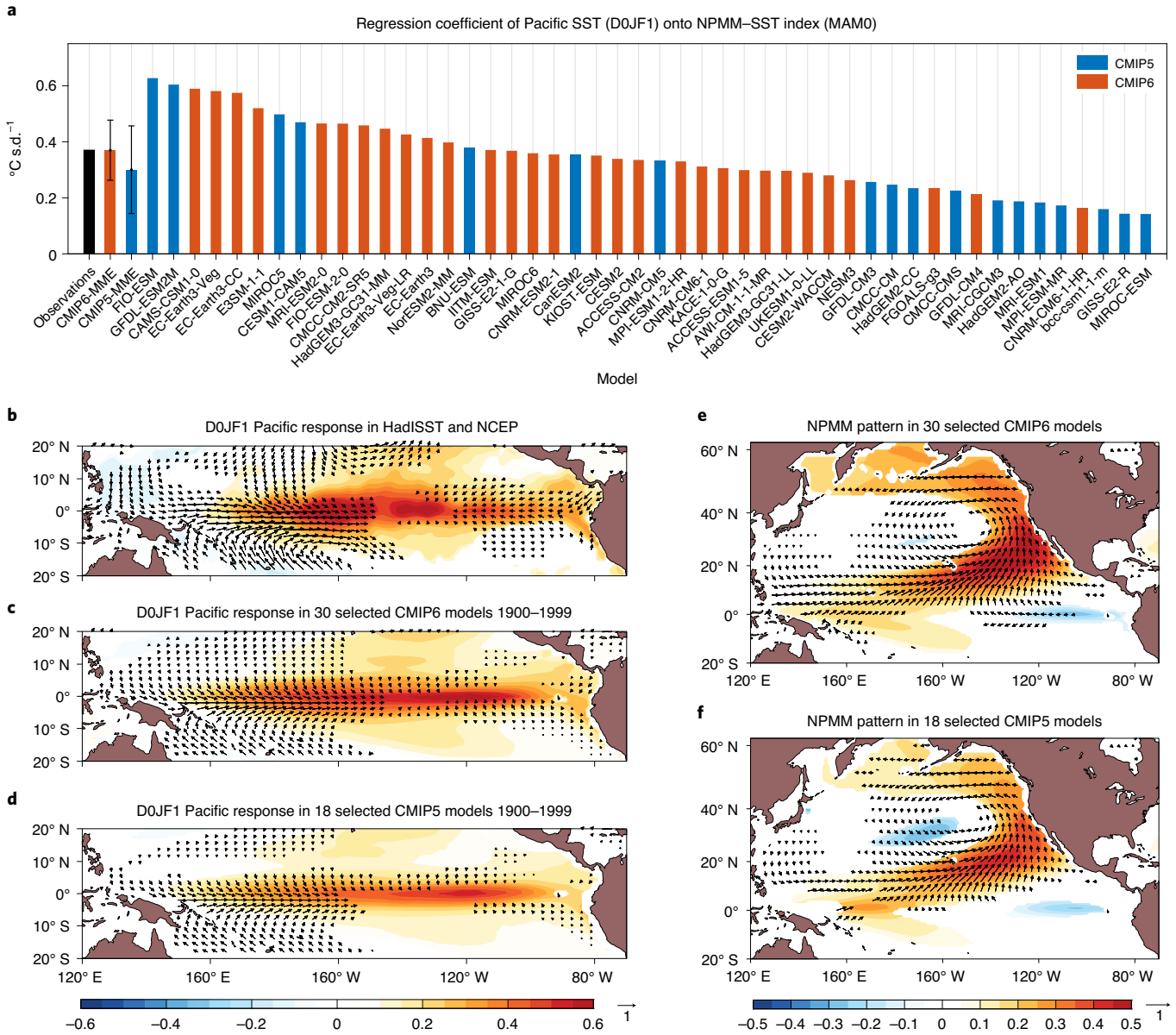


**Fig. 1 | Observed and modelled forcing of the NPMM on ENSO. a**, Equatorial Pacific SST response (°C s.d.$^{-1}$) to the NPMM over the 1948–2018 period in observations (black bar) and over the 1900–1999 period in CMIP5 (blue bars) and CMIP6 (orange bars) models, measured by area-averaged regression coefficients of the grid-point D0JF1 equatorial Pacific SST anomalies (5° S–5° N, 140° E–80° W) onto the normalized MAM0-averaged NPMM–SST index (see Sign-dependent average in Methods). A total of 18 CMIP5 and 30 CMIP6 models are able to produce statistically significant impact of the NPMM on the equatorial Pacific, and these 48 models are selected. **b**–**d**, Spatial pattern of the Pacific response by regression of D0JF1 tropical Pacific SST (°C s.d.$^{-1}$; shaded) and 10 m wind (m s$^{-1}$ s.d.$^{-1}$; vectors) anomalies onto the normalized MAM0-averaged NPMM–SST index based on observations (**b**) and multimodel average of the 30 selected CMIP6 models (**c**) and 18 selected CMIP5 models (**d**). **e**,**f**, NPMM spatial pattern by regression of monthly SST (shaded) and 10 m wind (vectors) anomalies onto the monthly NPMM–SST index based on the multimodel average of the 30 selected CMIP6 (**e**) and 18 selected CMIP5 (**f**) models. Error bars in **a** indicate the respective multimodel s.d. of the selected models. Values more than the 95% confidence level in **b** or the most robust features of ensemble where the mean exceeds 1.0 s.d. in **c**–**f** are shown. Colour bars in **b**–**d**,**e**,**f** represent regression coefficients (°C s.d.$^{-1}$).

We assess the ability of CMIP5 and CMIP6 models to reproduce the observed NPMM characteristics in their historical simulations over the 1900–1999 period, hereafter referred to as the present-day climate (see Model assessment in Methods). The modelled spatial pattern, intensity and coupling strength of the NPMM are generally comparable to those in the observations, although bias exists (Supplementary Fig. 2a–c). The CMIP5 and CMIP6 models also correctly simulate the seasonality of the NPMM, with the monthly variance of the NPMM–SST index peaking in boreal spring (Match, April and May (MAM0, where '0' refers to current year)) (Supplementary Fig. 2d–f). On a multimodel ensemble basis, the representation of the NPMM is improved from CMIP5 to CMIP6, especially in the simulation of NPMM spatial pattern and intensity.

Given that ENSO peaks in boreal winter (December, January and February (D0JF1, where '1' refers to the following year)), we measure the impact of the NPMM forcing on ENSO by a lagged regression of the grid-point D0JF1 equatorial Pacific SST anomalies (5° S–5° N, 140° E–80° W) onto the normalized MAM0-averaged NPMM–SST index, yielding the response of the equatorial Pacific grid-point SST. The impact is then evaluated by an average of the

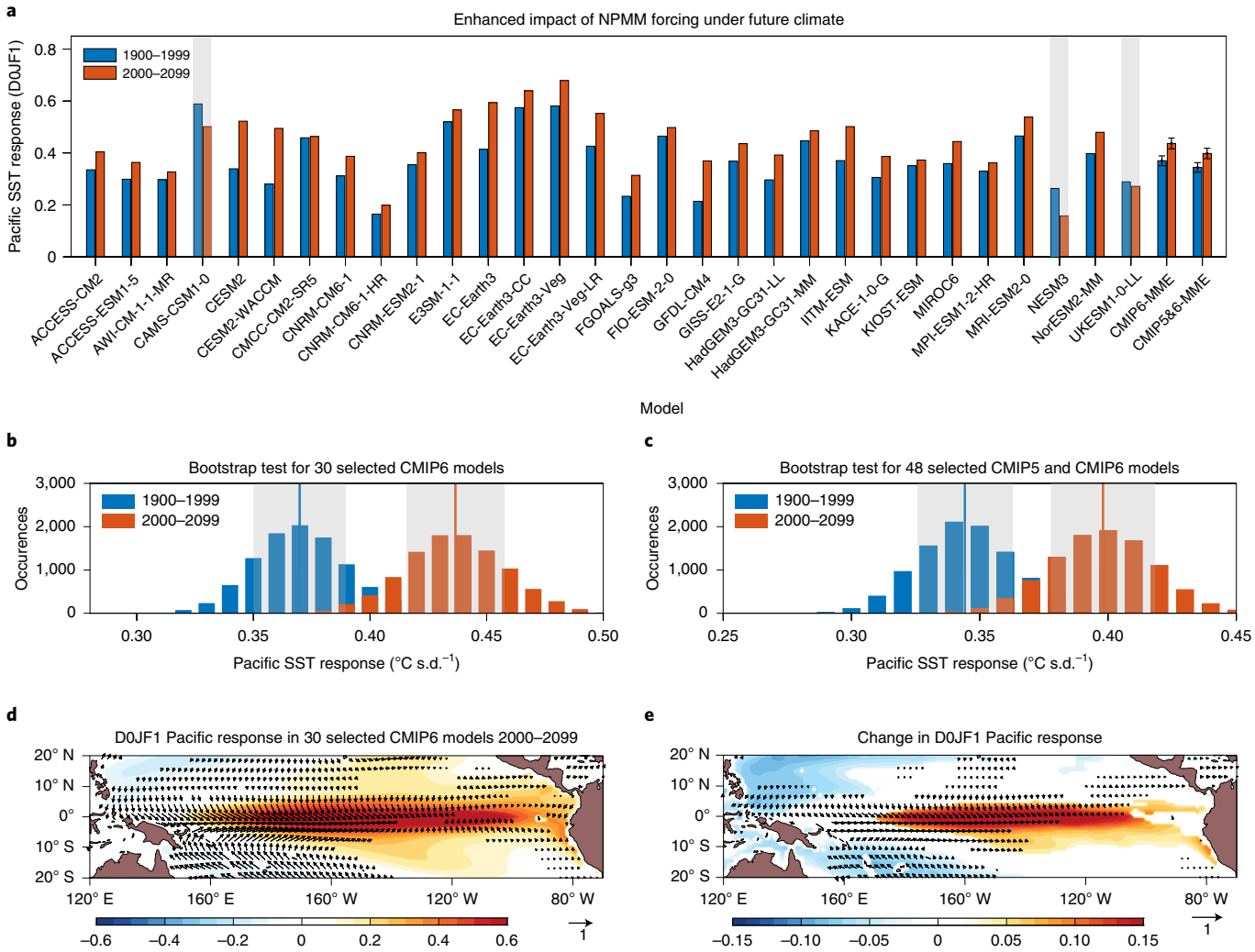


**Fig. 2 | Enhanced impact of the NPMM forcing on ENSO under greenhouse warming. a**, Comparison of the D0JF1 equatorial Pacific SST response under 100-year present-day (1900–1999; blue bars) and future (2000–2099; orange bars) climate in the 30 selected CMIP6 models. The multimodel mean and corresponding error bars for the CMIP6 models (labelled CMIP6-MME) and for the 48 selected CMIP5 and CMIP6 models combined (labelled CMIP5&6-MME) are also shown. Error bars are calculated as 1.0 s.d. of 10,000 inter-realizations of a bootstrap method (see Bootstrap test in Methods). Three models that simulate a decreased connection are greyed out. **b**,**c**, Histograms of 10,000 realizations of a bootstrap method for the Pacific SST response in the CMIP6 models (**b**) and in the CMIP5 and CMIP6 models combined (**c**). Blue and orange vertical lines indicate the mean values of 10,000 inter-realizations for the present-day and future periods, respectively. The grey shaded regions indicate the respective 1.0 s.d. of the 10,000 inter-realizations. **d**, Multimodel-mean spatial pattern of the D0JF1 Pacific response to the NPMM under future climate of the 30 selected CMIP6 models, obtained as for the present-day climate shown in Fig. 1c. **e**, Multimodel mean change in the D0JF1 Pacific response pattern between the future and present-day periods using the 30 selected CMIP6 models. Only the mean that exceeds 1.0 s.d. in **d**, or the change that is statistically significant above the 95% confidence level as determined by a two-sided Student's *t* test in **e**, is shown. Colour bars in **d**,**e** represent regression coefficients (°C s.d.$^{-1}$).

regression coefficients over grid points that are statistically significant (see Sign-dependent average in Methods). Hereafter, the preceding ENSO signal is removed from all the fields by linear regression onto the D–1JF0 (where '−1' refers to the preceding year) CTI index before the lagged regression analysis.

A total of 48 models (18 CMIP5 and 30 CMIP6 models) simulate a warming response in the central and eastern equatorial Pacific to a positive NPMM (Fig. 1a) under the present-day climate, and these 48 models are selected. A larger proportion of the CMIP6 models (30 of 42 models, or 71.4%; orange bars in Fig. 1a) reproduce the NPMM forcing on ENSO than that in CMIP5 (18 of 36 models, or 50.0%; blue bars in Fig. 1a). The multimodel mean response averaged over the equatorial Pacific in the 30 selected CMIP6 models ($0.37 \pm 0.10$ °C s.d.$^{-1}$) is close to the observed ($0.36$ °C s.d.$^{-1}$). However, the response in the 18 selected CMIP5 models ($0.30 \pm 0.16$ °C s.d.$^{-1}$) is 16.7% weaker.

The simulated spatial pattern of the D0JF1 Pacific response (Fig. 1b–d) and the NPMM pattern (compare Fig. 1e,f and Supplementary Fig. 1a) are comparable to the observed but are more realistic in CMIP6 (Fig. 1b,c) than in CMIP5 (Fig. 1b,d). Overall, the selected models produce the observed NPMM–ENSO connection; that is, a positive NPMM leads to an El Niño and the associated coupled oceanic–atmospheric processes involving the WES feedback and Bjerknes feedback[37] (Supplementary Fig. 3).

We focus on results from CMIP6 models because of their overall higher skill. To test the robustness of our conclusions in terms of a sensitivity to ensemble member size, we also present the results using all 48 selected CMIP5 and CMIP6 models combined.

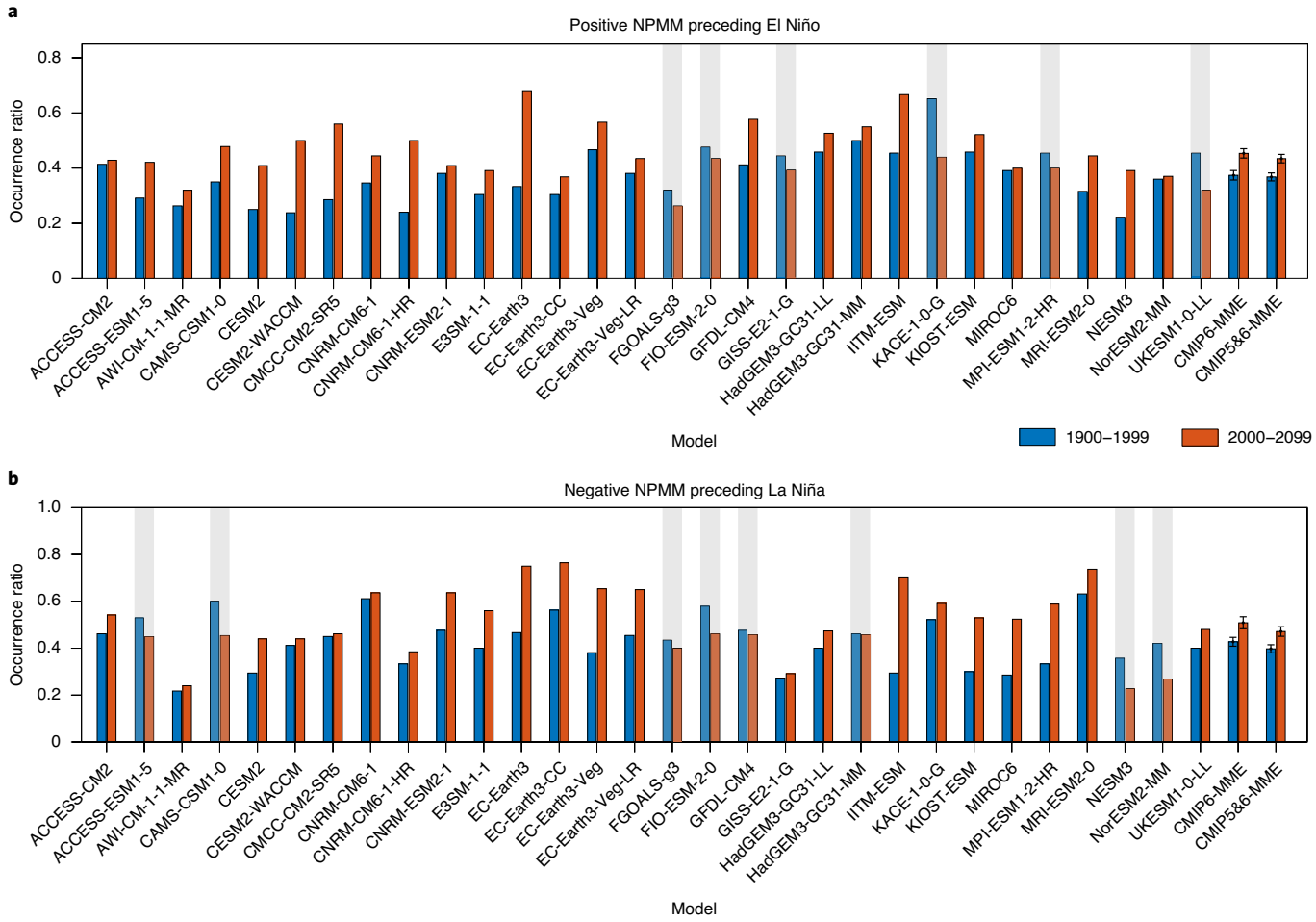


**Fig. 3 | Stronger impact of the NPMM on ENSO in the future climate. a**,**b**, Comparison of an occurrence ratio of positive NPMM events (NPMM–SST index > 0.75 s.d.) preceding El Niño (Niño3.4 index > 0.75 s.d.) over total positive NPMM events (**a**) and negative NPMM events (NPMM–SST index < −0.75 s.d.) preceding La Niña (Niño3.4 index < −0.75 s.d.) over total negative NPMM events (**b**) for the present-day (1900–1999; blue bars) and future (2000–2099; orange bars) periods in the 30 selected CMIP6 models. The multimodel mean and corresponding error bars for the CMIP6-MME and CMIP5&6-MME are also shown. Error bars are calculated as 1.0 s.d. of 10,000 inter-realizations of a bootstrap method (see Bootstrap test in Methods). Models that simulate a decrease in the occurrence ratio are greyed out.

We begin by showing that future NPMM is more impactful in forcing ENSO.

## Stronger NPMM impact on ENSO under greenhouse warming

We apply lagged regression of quadratically detrended D0JF1 SST anomalies onto the respective MAM0-averaged NPMM–SST index over the present-day (1900–1999) and future (2000–2099) period to obtain the average of significant regression coefficients over the equatorial Pacific (see Sign-dependent average in Methods). A total of 27 of the 30 selected CMIP6 models (90.0%) produce an enhanced response to the NPMM (Fig. 2a). The multimodel mean increase is 18.9%, from 0.37 °C s.d.$^{-1}$ in the present-day climate to 0.44 °C s.d.$^{-1}$ in the future climate. This increase is statistically significant above the 95% confidence level (Fig. 2b), according to a bootstrap method (see Bootstrap test in Methods). When the 18 selected CMIP5 models are included, a strong inter-model consensus persists, with 39 of the 48 models (81.3%) simulating an increase. The 48-model mean increase is 17.7%, again statistically significant above the 95% confidence level (Fig. 2c). The enhanced impact of the NPMM is supported by a comparison between the D0JF1 Pacific response patterns over the two periods (Figs. 1c and 2d), showing stronger warm SST and westerly wind anomalies in the equatorial western and central Pacific under future climate (Fig. 2e).

Associated with the enhanced NPMM forcing, there is an increase in NPMM events that precede ENSO events. Here we use 0.75 s.d. of the NPMM–SST index as a threshold to define NPMM events and 0.75 s.d. of the Niño3.4 index to define ENSO events; the result is insensitive to the threshold for ENSO definition used (Supplementary Fig. 4a). Under future climate, there is an increased occurrence ratio in terms of positive NPMM events preceding El Niño events over the total positive NPMM events (Fig. 3a; 24 of the 30 models, or 80.0%, generating an increase) and negative NPMM events preceding La Niña events over the total negative NPMM events (Fig. 3b; 22 of the 30 models, or 73.3%, generating an increase). When the CMIP5 and CMIP6 models are combined, a statistically significant increase in the occurrence ratio persists underpinned by a strong inter-model consensus, with 75.0% (70.8%) of the models generating the increase in terms of a positive (negative) NPMM preceding an El Niño (a La Niña).

For extreme ENSO events that exert severe impacts, the increased NPMM forcing on ENSO under greenhouse warming is particularly conspicuous. The occurrence ratio of positive NPMM events preceding extreme El Niño (defined by E-index > 1.5 s.d., as in ref. [38])

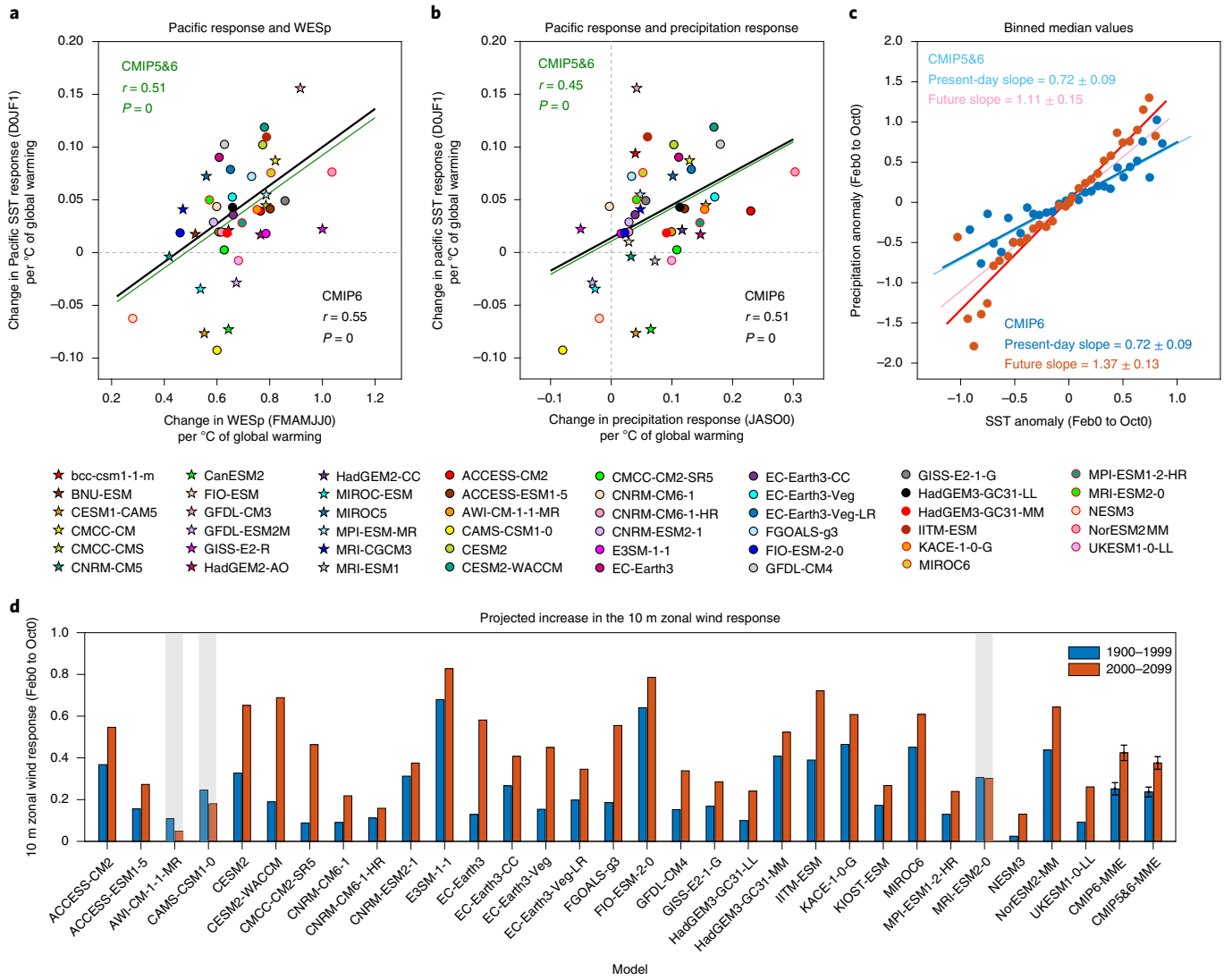


**Fig. 4 | Mechanism for the stronger NPMM forcing on ENSO. a**,**b**, Inter-model relationship between the change (future minus present-day) of the DOJF1 equatorial Pacific SST response (*y* axis; °C s.d.$^{-1}$ °C$^{-1}$) with WESp (W s m$^{-3}$ °C$^{-1}$) (**a**) and with summer deep convection response (mm d$^{-1}$ s.d.$^{-1}$ °C$^{-1}$) (**b**). The CMIP5 and CMIP6 models are denoted by stars and dots, respectively, using models in which data are available (see Observed and CMIP5/6 data in Methods). Linear fit is displayed together with correlation coefficient *r* and *P* value based on the 30 selected CMIP6 models (black line and black text) and the 48 selected CMIP5 and CMIP6 models combined (green line and green text). Changes in each model are scaled by the corresponding increase in global mean temperature. **c**, Responses of FMAMJJASO0 precipitation anomalies (mm d$^{-1}$) to FMAMJJASO0 SST anomalies using the 30 CMIP6 models alone and the 48 CMIP5 and CMIP6 models combined over the subtropical Pacific (5° N–25° N, 160° E–120° W), in the present-day (blue dots) and future (orange dots) 100-year periods. The precipitation anomalies are binned in 0.05 °C SST anomaly intervals to obtain median anomaly in each bin first. Linear fits are provided, similar to **a** and **b**, for CMIP6 alone (thick line) and CMIP5 and CMIP6 combined (thin line). **d**, Same as in Fig. 2a but for a comparison of the 10 m FMAMJJASO0 zonal wind response (m s$^{-1}$ s.d.$^{-1}$) to the normalized MAM0 NPMM–SST index averaged over the equatorial western Pacific (5° S–5° N, 140° E–160° W).

and negative NPMM events preceding extreme La Niña (defined by C-index < −1.75 s.d., as in ref. [1]) increase in 73.3% and 66.7%, respectively, of the 30 selected CMIP6 models (Supplementary Fig. 4b,c) (see E-index and C-index in Methods). In aggregation, there is a 58.3% increase in the relationship between positive NPMM and extreme El Niño, from 12 per 100 positive NPMM events that precede extreme El Niño under present-day climate to 19 per 100 positive NPMM events that precede extreme El Niño under future climate (Supplementary Fig. 4b); likewise, there is a 75.0% increase in the relationship between negative NPMM and extreme La Niña, from 12 per 100 negative NPMM events preceding extreme La Niña under present-day climate to 21 per 100 negative NPMM events preceding extreme La Niña under future climate (Supplementary Fig. 4c). With the 18 selected CMIP5 models added, the conclusion remains. Thus, the enhanced NPMM forcing leads to an increased frequency of extreme ENSO events.

## Enhanced thermodynamic feedbacks under greenhouse warming

Mechanisms for the increased NPMM impact on ENSO lie in an increased efficacy of thermodynamic feedbacks associated with the NPMM. In the following, we show that there is a lack of an inter-model consensus on a change in the NPMM intensity per se, especially in the subtropical Pacific (Supplementary Figs. 5a–c and 6a) despite an increase in some models reported earlier[39]. Further, there is a lack of impact from changes in trade-wind charging

mechanism[40] (Supplementary Fig. 6b). Instead, the increased NPMM impact on ENSO is due to an enhanced WES feedback[3,5,6] and summer deep convection response[19] under greenhouse warming.

## Enhanced WES feedback

The NPMM-related SST and surface wind anomalies propagate to the equatorial western and central Pacific during boreal spring and early summer (FMAMJJ0) through the WES feedback[3,5,6]. These surface anomalies trigger Bjerknes positive feedback and induce ENSO development in the ensuing seasons. We use change in latent heat flux per unit change in zonal wind speed to estimate the intensity of the WES feedback as in previous studies[5,41–43], referred to as a WES parameter (WESp) (see WES parameter and decomposition in Methods). The WESp in the future climate increases over the subtropical Pacific (Supplementary Fig. 5d–f), covering the main NPMM pathway (5° N–25° N, 160° E–130°W) to the tropical Pacific. This increased WESp is simulated in all 30 models (Fig. 4a), and models that generate a larger increase in the FMAMJJ0 WESp tend to simulate a stronger D0JF1 Pacific SST response. The inter-model correlation is statistically significant ($r=0.55$, $P<0.001$), indicating that the more intense WES feedback acts as one important mechanism for the greater NPMM impact in forcing ENSO.

Changes in the WESp can be induced by changes in the wind speed, relative humidity, SST and air–sea surface temperature difference (see WES parameter and decomposition in Methods). The decomposition finds that the changing SST term dominates the changing WESp decomposition in all models, suggesting that the increased WESp in the future climate comes mainly from the increased background SST (Supplementary Fig. 7a,b). This is despite part of the reinforcing effect being offset by a basin-wide increase in the relative humidity and a decrease in the air–sea surface temperature difference (blue and cyan bars in Supplementary Fig. 7a, respectively; Supplementary Fig. 7c,d). Further, stronger mean zonal wind would lead to a more intense WES feedback, and vice versa[26,43], but there is no inter-model consensus on changes in the zonal wind over the subtropical Pacific (Supplementary Fig. 7a,e). Thus, the rising mean SST is a dominating forcing for the enhanced WES feedback.

## Stronger summer deep convection response

After boreal spring/early summer, the inter-tropical convergence zone moves northward and interacts with the NPMM-related SST anomalies in the subtropical Pacific, causing a Gill-type atmospheric response that projects surface wind anomalies onto the Equator for the second time. Referred to as a summer deep convection response[19], the associated wind anomalies offer another opportunity for the NPMM to influence the tropical Pacific and ENSO. We measure the summer deep convection response by regression of late boreal summer/early fall (JASO0) precipitation anomalies onto the normalized MAM0-averaged NPMM–SST index. The summer deep convection response features a cyclonic circulation and positive precipitation anomalies over the subtropical Pacific (Supplementary Figs. 3c and 5g). Under greenhouse warming, the summer deep convection response shows a general enhancement, especially west of the dateline (Supplementary Fig. 5h,i), with 26 of the 30 models (86.7%) producing a stronger precipitation response to the NPMM (Fig. 4b). The stronger summer deep convection response is significantly positively correlated ($r=0.51$, $P<0.001$) with the stronger D0JF1 Pacific SST response. Hence, the stronger summer deep convection response also contributes to the enhanced NPMM forcing.

## Negligible impact from trade-wind charging

NPMM-related boreal-winter and spring extratropical wind-stress curl anomalies can induce a charge (discharge) of the ocean heat content (trade-wind charging)[40], facilitating the onset of El Niño (La Niña) events. We measure this process by regression of FMA0 wind-stress curl anomalies onto the normalized MAM0-averaged NPMM–SST index. There is a significant weakening in the multimodel response of off-equatorial wind-stress curl to the NPMM from the present-day to future climate (Supplementary Fig. 5j–l). Meanwhile, there is little relationship between the inter-model changes in the wind-stress curl response and those in the Pacific SST response (Supplementary Fig. 6b). The enhanced impact of the NPMM forcing is thus unlikely to be induced by this mechanism.

Overall, the nonlinear relationship between evaporation and SST anomaly[44] under a warming background SST is of primary importance. In response to SST anomalies, larger precipitation anomalies are generated in the future than in the present-day climate, as indicated by different slopes for the two periods (Fig. 4c). It is the warmer subtropical local background SST that enhances both the WES feedback and the summer deep convection response, rather than a relative warming to the tropical region, a point underscored by a lack of inter-model relationship between SST warming patterns and changes in the two processes (Supplementary Fig. 6c,d). These two enhanced thermodynamic processes induce larger westerly wind anomalies in the equatorial western Pacific from early boreal spring to early boreal fall (February to October) (Fig. 4d), manifested as a statistically significant strengthening in the response of westerlies to the MAM0-averaged NPMM–SST index, by as much as 68.0%. The stronger wind response is seen over the entire nine months (Supplementary Fig. 8). These larger westerly wind anomalies are conducive to an El Niño-like condition in the ensuing winter by triggering oceanic Kelvin waves and Bjerknes positive feedback, hence an enhanced NPMM–ENSO connection. These results hold when the 18 selected CMIP5 models are included (green lines and green text of Fig. 4a,b; light blue and pink lines and text of Fig. 4c).

## Negligible impacts from mean state change and model bias

The equatorial Pacific mean state is projected to change under greenhouse warming[1], which seems less important in the enhanced NPMM forcing on ENSO (Supplementary Fig. 9a). An inter-model correlation between changes of the D0JF1 Pacific SST response and changes of equatorial Pacific climatological SST shows an overall lack of a statistically significant relationship (correlation $<-0.1$) except over a small area of far-eastern Pacific around 90° W (correlation $<0.35$), supporting the importance of the enhanced subtropical processes in the intensified NPMM–ENSO connection. There is no evidence to suggest that either the model cold tongue bias (Supplementary Fig. 9b) or the bias of NPMM–ENSO connection itself (Supplementary Fig. 9c) contributes to the enhanced future Pacific SST response.

## Enhanced NPMM impact in an intermediate climate model

We further demonstrate the increased NPMM impact in an intermediate climate model (see Intermediate model description in Methods). This model has been used to study NPMM or climate change-related issues[4,11,45]. We perform two sets of 30-member initial-value ensemble runs based on the common equilibrium state of long-time integrated CTRL (constant $CO_2$ concentration of 355 ppm; Methods) and $4\times CO_2$ (1,420 ppm; Methods) with slightly different initial conditions. For each member, the observed positive NPMM SST pattern (Supplementary Fig. 1a) amplified by a factor of 4 (to increase a response signal) is initiated over the subtropical Pacific on the first day of March for 24 h and tracked for one year within the fully coupled environment (see Single-model ensemble experiments in Methods).

The initial experiments under CTRL reproduce the NPMM–ENSO relationship in the multimember ensemble mean. A positive NPMM SST anomaly in boreal spring induces an El Niño-like Pacific response in the ensuing winter (Fig. 5a), although the warm

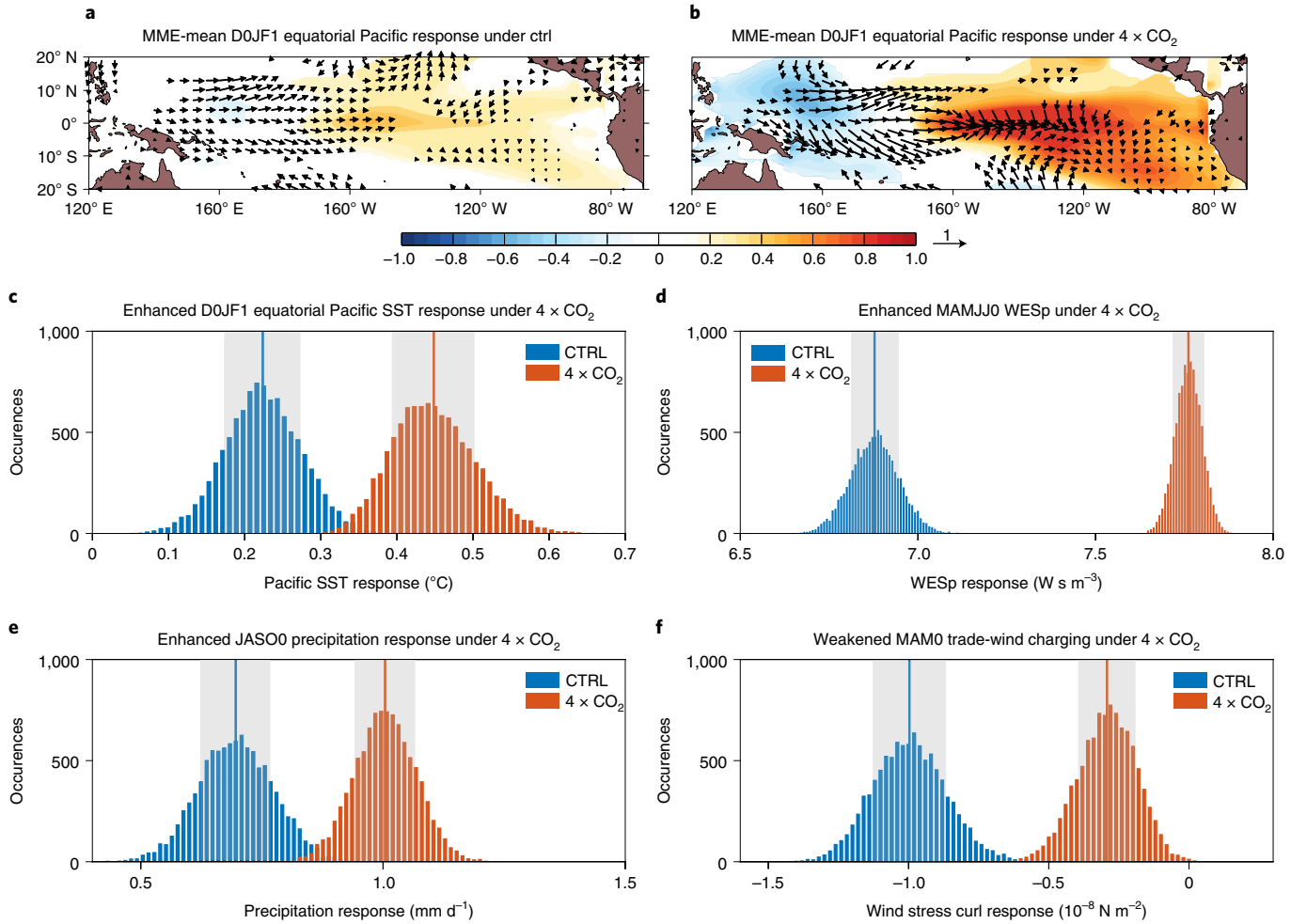


**Fig. 5 | Enhanced impact of the NPMM forcing on ENSO in a single-model ensemble experiment. a**,**b**, Multimember ensemble mean of the D0JF1 SST and 10 m wind responses to SST forcing of a positive NPMM in the initial experiments under CTRL (**a**) and 4 × $CO_2$ (**b**) conditions (see Single-model ensemble experiments in Methods). Only responses that exceed 1.0 s.d. are shown. Colour bar represents SST anomalies (°C). **c**–**f**, Histograms of 10,000 realizations of a bootstrap method (see Bootstrap test in Methods) for the Pacific SST response (**c**), background WESp (**d**), summer deep convection response (**e**) and trade-wind charging mechanism (**f**) in the initial experiments under CTRL (blue) and 4 × $CO_2$ (orange). The Pacific SST response is measured by area-averaged D0JF1 equatorial Pacific (5° S–5° N, 160° E–90° W) SST anomalies. The background WESp is obtained by an average of WESp over the major path of the WES feedback (5° N–25° N, 160° E–130° W) during MAMJJ0. The summer deep convection response is measured by an average of JASO0 precipitation anomalies over the key region of summer deep convection (5° N–25° N, 150° E–130° W). The trade-wind charging mechanism is measured by an average of wind-stress curl anomalies over the key region of trade-wind charging (0° N–5° N, 170° E–120° W) during MAM0. Blue and orange vertical lines indicate mean values of 10,000 inter-realizations for the CTRL and 4 × $CO_2$, respectively. The grey shaded regions indicate the respective 1.0 s.d. of the 10,000 inter-realizations.

SST anomalies are more concentrated in the central Pacific comparing with the observed. This pattern agrees with many previous findings of a stronger statistical relationship between the NPMM and the CP ENSO events[7,18,19,25,26]. The same NPMM SST pattern under 4 × $CO_2$ causes stronger D0JF1 SST and wind anomalies over the equatorial Pacific (Fig. 5b). This enhanced response is statistically significant above the 95% confidence level based on a bootstrap test (Fig. 5c), with the multimember ensemble mean D0JF1 equatorial Pacific SST anomalies increasing from 0.22 °C under CTRL to 0.45 °C under 4 × $CO_2$. As in our analysis of CMIP5/6 models, both the WES feedback and the summer deep convection response strengthen significantly under 4 × $CO_2$ (Fig. 5d,e), enhancing the impact of the NPMM forcing under greenhouse warming. By contrast, the negative wind-stress curl response during MAM0 (trade-wind charging progress) weakens significantly under 4 × $CO_2$ (Fig. 5f), which is opposite to the stronger Pacific El Niño-like response during D0JF1.

## Conclusions

Forcing of ENSO by the NPMM becomes stronger under greenhouse warming. Both the WES feedback and summer deep convection response operate more effectively in a background of higher SSTs under future climate because evaporation is a nonlinear function of the background temperature. Consequently, the NPMM is more efficient in triggering ENSO events, including extreme El Niño and extreme La Niña events, by inducing larger surface wind anomalies over the equatorial western Pacific, despite little change in the NPMM amplitude. The enhanced impact and mechanism are supported by the intermediate climate model experiments, in which the same positive NPMM SST pattern induces a stronger El Niño-like response in a warming climate. Thus, the enhanced impact from subtropical North Pacific variability contributes to the projected increase in frequency of extreme ENSO events under greenhouse warming. Further, the enhanced impact means that subtropical North Pacific variability becomes a more influential

precursor for future ENSO prediction, offering an important avenue for increasing ENSO predictability that can help to alleviate the corresponding socioeconomic impact.

## Online content

Any methods, additional references, Nature Research reporting summaries, source data, extended data, supplementary information, acknowledgements, peer review information; details of author contributions and competing interests; and statements of data and code availability are available at https://doi.org/10.1038/s41558-021-01139-x.

Received: 1 April 2021; Accepted: 2 August 2021;
Published online: 16 September 2021

## References

1. Cai, W. et al. Butterfly effect and a self-modulating El Niño response to global warming. *Nature* **585**, 68–73 (2020).
2. Cai, W. et al. Climate impacts of the El Niño–Southern Oscillation on South America. *Nat. Rev. Earth Environ.* **1**, 215–231 (2020).
3. Chiang, J. C. H. & Vimont, D. J. Analogous Pacific and Atlantic meridional modes of tropical atmosphere–ocean variability. *J. Clim.* **17**, 4143–4158 (2004).
4. Chang, P. et al. Pacific meridional mode and El Niño–Southern Oscillation. *Geophys. Res. Lett.* **34**, L16608 (2007).
5. Vimont, D. J., Alexander, M. A. & Fontaine, A. Midlatitude excitation of tropical variability in the Pacific: the role of thermodynamic coupling and seasonality. *J. Clim.* **22**, 518–534 (2009).
6. Alexander, M. A., Vimont, D. J., Chang, P. & Scott, J. D. The impact of extratropical atmospheric variability on ENSO: testing the seasonal footprinting mechanism using coupled model experiments. *J. Clim.* **23**, 2885–2901 (2010).
7. Yu, J.-Y. & Kim, S. T. Relationships between extratropical sea level pressure variations and the Central-Pacific and Eastern-Pacific types of ENSO. *J. Clim.* **24**, 708–720 (2011).
8. Vimont, D. J., Battisti, D. S. & Hirst, A. C. Footprinting: a seasonal connection between the tropics and mid-latitudes. *Geophys. Res. Lett.* **28**, 3923–3926 (2001).
9. Xie, S.-P. & Philander, S. G. H. A coupled ocean–atmosphere model of relevance to the ITCZ in the eastern Pacific. *Tellus* **46A**, 340–350 (1994).
10. Stuecker, M. F. Revisiting the Pacific Meridional Mode. *Sci. Rep.* **8**, 3216 (2018).
11. Zhang, L., Chang, P. & Ji, L. Linking the Pacific Meridional Mode to ENSO: coupled model analysis. *J. Clim.* **22**, 3488–3505 (2009).
12. Larson, S. & Kirtman, B. P. The Pacific Meridional Mode as an ENSO precursor and predictor in the North American multimodel ensemble. *J. Clim.* **27**, 7018–7032 (2014).
13. Lin, C.-Y., Yu, J.-Y. & Hsu, H.-H. CMIP5 model simulations of the Pacific Meridional Mode and its connection to the two types of ENSO. *Int. J. Climatol.* **35**, 2352–2358 (2015).
14. Ma, J., Xie, S.-P. & Xu, H. Contributions of the North Pacific Meridional Mode to ensemble spread of ENSO prediction. *J. Clim.* **30**, 9167–9181 (2017).
15. Amaya, D. J. The Pacific Meridional Mode and ENSO: a review. *Curr. Clim. Change Rep.* **5**, 296–307 (2019).
16. Lu, F., Liu, Z., Liu, Y., Zhang, S. & Jacob, R. Understanding the control of extratropical atmospheric variability on ENSO using a coupled data assimilation approach. *Clim. Dyn.* **48**, 3139–3160 (2017).
17. Lu, F. & Liu, Z. Assessing extratropical influence on observed El Niño–Southern Oscillation events using regional coupled data assimilation. *J. Clim.* **31**, 8961–8969 (2018).
18. Vimont, D. J., Alexander, M. A. & Newman, M. Optimal growth of central and East Pacific ENSO events. *Geophys. Res. Lett.* **41**, 4027–4034 (2014).
19. Amaya, D. J. et al. The North Pacific pacemaker effect on historical ENSO and its mechanisms. *J. Clim.* **32**, 7643–7661 (2019).
20. Ashok, K., Behera, S. K., Rao, S. A., Weng, H. & Yamagata, T. El Niño Modoki and its possible teleconnection. *J. Geophys. Res.* **112**, C11007 (2007).
21. Kug, J.-S., Jin, F.-F. & An, S.-I. Two types of El Niño events: cold tongue El Niño and warm pool El Niño. *J. Clim.* **22**, 1499–1515 (2009).
22. Kao, H.-Y. & Yu, J.-Y. Contrasting Eastern-Pacific and Central-Pacific types of ENSO. *J. Clim.* **22**, 615–632 (2009).
23. Yu, J. -Y. & Fang, S.-W. The distinct contributions of the seasonal footprinting and charged–discharged mechanisms to ENSO complexity. *Geophys. Res. Lett.* **45**, 6611–6618 (2018).
24. Fang, S.-W. & Yu, J. -Y. Contrasting transition complexity between El Niño and La Niña: observations and CMIP5/6 models. *Geophys. Res. Lett.* **47**, e2020GL088926 (2020).
25. Yu, J.-Y., Kao, H.-Y. & Lee, T. Subtropics-related interannual sea surface temperature variability in the central equatorial Pacific. *J. Clim.* **23**, 2869–2884 (2010).
26. Yu, J.-Y. et al. Linking emergence of the Central-Pacific El Niño to the Atlantic Multi-decadal Oscillation. *J. Clim.* **28**, 651–662 (2015).
27. Hu, Z.-Z., Kumar, A., Huang, B., Zhu, J. & Yu, J.-Y. The interdecadal shift of ENSO properties in 1999/2000: a review. *J. Clim.* **33**, 4441–4462 (2020).
28. Capotondi, A. & Sardeshmukh, P. D. Optimal precursors of different types of ENSO events. *Geophys. Res. Lett.* **42**, 9952–9960 (2015).
29. Zhang, H., Clement, A. & Di Nezio, P. The South Pacific Meridional Mode: a mechanism for ENSO-like variability. *J. Clim.* **27**, 769–783 (2014).
30. Min, Q., Su, J., Zhang, R. & Rong, X. What hindered the El Niño pattern in 2014? *Geophys. Res. Lett.* **42**, 6762–6770 (2015).
31. Min, Q., Su, J., Zhang, R. & Rong, X. Impact of the South and North Pacific meridional modes on the El Niño–Southern Oscillation: observational analysis and comparison. *J. Clim.* **30**, 1705–1720 (2017).
32. You, Y. & Furtado, J. C. The South Pacific Meridional Mode and its role in tropical Pacific climate variability. *J. Clim.* **31**, 10141–10163 (2018).
33. Liguori, G. & Di Lorenzo, E. Separating the North and South Pacific meridional modes contributions to ENSO and tropical decadal variability. *Geophys. Res. Lett.* **46**, 906–915 (2019).
34. Di Lorenzo, E. et al. ENSO and meridional modes: a null hypothesis for Pacific climate variability. *Geophys. Res. Lett.* **42**, 9440–9448 (2015).
35. Zhao, Y. & Di Lorenzo, E. The impacts of extra-tropical ENSO precursors on tropical Pacific decadal-scale variability. *Sci. Rep.* **10**, 3031 (2020).
36. Pegion, K., Selman, C. M., Larson, S. M., Furtado, J. C. & Becker, E. J. The impact of the extratropics on ENSO diversity and predictability. *Clim. Dyn.* **54**, 4469–4484 (2020).
37. Bjerknes, J. Atmospheric teleconnections from the equatorial Pacific. *Mon. Weather Rev.* **97**, 163–172 (1969).
38. Cai, W. et al. Increased variability of eastern Pacific El Niño under greenhouse warming. *Nature* **564**, 201–206 (2018).
39. Liguori, G. & Di Lorenzo, E. Meridional modes and increasing Pacific decadal variability under anthropogenic forcing. *Geophys. Res. Lett.* **45**, 983–991 (2018).
40. Anderson, B. T., Perez, R. C. & Karspeck, A. Triggering of El Niño onset through trade wind-induced charging of the equatorial Pacific. *Geophys. Res. Lett.* **40**, 1212–1216 (2013).
41. Czaja, A., van der Vaart, P. & Marshall, J. A diagnostic study of the role of remote forcing in tropical Atlantic variability. *J. Clim.* **15**, 3280–3290 (2002).
42. Vimont, D. J. Transient growth of thermodynamically coupled variations in the tropics under an equatorially symmetric mean state. *J. Clim.* **23**, 5771–5789 (2010).
43. Sanchez, S. C., Amaya, D. J., Miller, A. J., Xie, S.-P. & Charles, C. D. The Pacific Meridional Mode over the last millennium. *Clim. Dyn.* **53**, 3547–3560 (2019).
44. Gill, A. E. Some simple solutions for heat-induced tropical circulation. *Q. J. R. Meteorol. Soc.* **106**, 447–462 (1980).
45. Jia, F. et al. Weakening Atlantic Niño–Pacific connection under greenhouse warming. *Sci. Adv.* **5**, eaax4111 (2019).

## Methods

**Observed and CMIP5/6 data.** The observed monthly SST and atmospheric fields (three-dimensional velocities, heat flux, relative humidity, surface air temperature and precipitation) covering the 1948–2018 period are from the Hadley Centre Sea Ice and Sea Surface Temperature (HadISST) dataset[46] and the National Center for Environmental Prediction (NCEP)/National Center for Atmospheric Research (NCAR) reanalysis 1 (ref. [47]), respectively. We examine monthly outputs over the 1900–2099 period from 36 CMIP5 models forced by historical forcing up to 2005 and thereafter representative concentration pathway (RCP) 8.5 scenario (an escalating radiative force throughout the twenty-first century, reaching approximately 8.5 W m$^{-2}$ in 2100)[48] and 42 CMIP6 models forced by historical forcing up to 2014 and thereafter Shared Socioeconomic Pathway (SSP) 5–8.5 scenario (approximately equivalent to RCP 8.5)[49]. One ensemble member of each model is used, which is r1i1p1 in CMIP5 and mostly r1i1p1f1 in CMIP6 (Supplementary Table 1). We compare the NPMM forcing on ENSO between the 1900–1999 period (present-day climate) and the 2000–2099 period (future climate). All the observational and modelling data are interpolated to a 1°×1° grid. Anomalies in this study are computed by removing seasonal cycles and quadratic trends from the monthly data.

The anomalies in CMIP5 and CMIP6 outputs are obtained on the basis of the full 200-year period (1900–2099). Four models (bcc-csm1-1-m, MRI-ESM1, FIO-ESM and KIOST-ESM) are not involved in Fig. 4a, Supplementary Fig. 6c and Supplementary Fig. 7 as the total wind-speed data of the first three models and the latent heat-flux data of KIOST-ESM are unavailable. KIOST-ESM is not involved in Fig. 4b,c and Supplementary Fig. 6d as the precipitation data are unavailable. There is no evidence to suggest that results from the 78 CMIP5 and CMIP6 models are dependent samples; due to butterfly effects[1], even results from large ensemble experiments with the same model can be treated as independent realizations.

**Depiction of the NPMM.** The NPMM is obtained by applying an MCA to quadratically detrended monthly SST and 10 m wind anomalies over the Pacific Ocean (21° S–32° N, 175° E–95° W) in observations and models[3]. The NPMM temporal variation is described by the normalized monthly SST and wind expansion coefficients of the MCA (NPMM–SST and NPMM–wind index, respectively), and the NPMM spatial pattern is obtained by linear regression of the SST and 10 m wind anomalies onto the NPMM–SST index. We use the NPMM–SST index to study the NPMM–ENSO connection as this index is more representative of the coupled mode[3]. By contrast, the NPMM–wind index mixes the atmospheric variance of both the internal NPMM mode and external forcing (such as the North Pacific Oscillation).

As commonly used in previous studies[3,13,15,31–33,39], the ENSO signal is removed by linear regression onto the monthly CTI (SST anomalies averaged in the region of 6° S–6° N, 180°–90° W) before the MCA analysis or onto the D–1JF0 CTI index before the regression analysis. The ENSO signal has been largely removed by this approach since the largest simultaneous correlation coefficient between the NPMM–SST index and CTI is less than 0.15 for the CMIP5 and CMIP6 models. Considering that the ENSO may lead the NPMM in some models, we also recompute the NPMM in the 48 selected models by removing (linear regression) both the simultaneous CTI and the four-month leading CTI before the MCA analysis. Although the detailed NPMM index of each model is slightly different between the two MCA analyses, our conclusions, including the enhanced impact of the NPMM forcing and the more efficient thermodynamic processes, do not change.

For CMIP5 and CMIP6 models, the MCA is applied to the full 200-year period (1900–2099) to represent the overall simulations of NPMM in both the present-day and future climates. Although the NPMM is the leading MCA mode (MCA1) of subtropical north Pacific (after removing ENSO) in observations, it may appear as the second mode (MCA2) in some climate models. Therefore, we compare the SST patterns of the leading two MCA modes in each model's historical simulation (1900–1999) with the observed MCA1 SST pattern (20° S–32° N, 140° E–80° W), taking the MCA mode that has a larger pattern correlation coefficient (closer to the observed pattern) to be the model's NPMM. Using this method, six CMIP5 models and six CMIP6 models have their NPMMs captured by MCA2, with the remaining models by MCA1 (Supplementary Table 1).

**Model assessment.** We use four metrics to examine the ability of CMIP5/6 models to reproduce the observed NPMM properties in the present-day climate, including an NPMM pattern correlation, an NPMM intensity, an NPMM coupling strength and an NPMM seasonality. The multimodel-mean pattern correlation (Supplementary Fig. 2a) of NPMM SST variability in CMIP6 (0.78) is higher than that in CMIP5 (0.71), associated with a 27.3% smaller inter-model spread (0.16) comparing with CMIP5 models (0.22). The NPMM intensity is measured by an average of SST regression coefficients in the southwest of Baja California (black box in Supplementary Fig. 1a), where the largest SST anomalies of NPMM exist. There are more models in CMIP6 simulating a reasonable NPMM intensity than models in CMIP5 (Supplementary Fig. 2b). A total of 21 of the 36 (58.3%) CMIP5 models and 35 of the 42 (83.3%) CMIP6 models have correlation coefficients larger than 0.7, indicating that the NPMM spatial pattern is more reasonably simulated in CMIP6 than in CMIP5. Compared with the observation (0.41 °C s.d.$^{-1}$), a total of 29 of the 36 (80.6%) CMIP5 models underestimate the NPMM intensity (multimodel mean: 0.34 ± 0.09 °C s.d.$^{-1}$). By contrast, the multimodel average (0.41 ± 0.09 °C s.d.$^{-1}$) of CMIP6 is identical to the observed, although the inter-model spread remains unchanged.

Air–sea coupling processes are fundamental to development of the NPMM, which is measured by a correlation between the respective NPMM–SST and NPMM–wind indices (Supplementary Fig. 2c). The NPMM coupling strength is underestimated in CMIP5 and CMIP6, with 23 of the 36 (63.9%) CMIP5 models and 32 of the 42 (76.2%) CMIP6 models generating a weaker NPMM coupling strength than the observed correlation of 0.75. However, considering observational uncertainty, the multimodel mean coupling strength is still in a reasonable range (0.72 ± 0.08 in CMIP5 and 0.71 ± 0.07 in CMIP6). The seasonality of the NPMM is reasonably well simulated by the CMIP5 and CMIP6 models (Supplementary Fig. 2d–f), with monthly s.d. of the NPMM–SST index peaking in MAM0 and the NPMM–wind index peaking one month earlier. Overall, the representation of the NPMM improves from CMIP5 to CMIP6 on a multimodel ensemble average. The NPMM simulated by the CMIP5/6 models is generally comparable to that in the observation, although model bias exists. Together with the result of Fig. 1a, it suggests an improvement in simulating the NPMM–ENSO connection in CMIP6 climate models.

**Sign-dependent average.** The regression coefficients in the equatorial Pacific (5° S–5° N, 140° E–80° W) are averaged as follows[45]. First, we consider and average only the regression coefficients at grid points that are statistically significant (more than the 95% confidence level). Second, the sign of the averaged value is checked. If the sign is positive (negative), then only the significant positive (negative) coefficients are averaged. If all the regression coefficients in the equatorial Pacific grid points are insignificant, the value is set to zero. This method is adapted to avoid an offset between the positive and negative values.

**Bootstrap test.** A bootstrap method[50] is used to examine whether the multimodel mean enhancement in the D0JF1 Pacific SST response is statistically significant[38,45]. The 30 response values in the present-day period (blue bars in Fig. 2a) are resampled randomly to construct 10,000 realizations of mean response value over 30 models. In this random resampling process, any response value can be selected again. The same is carried out for the future period (orange bars in Fig. 2a). We compute the s.d. of the 10,000 inter-realizations of mean response value for the two periods, which is 0.019 °C s.d.$^{-1}$ and 0.021 °C s.d.$^{-1}$, respectively. The increased mean response in the future period (0.07 °C s.d.$^{-1}$) is greater than the sum of these two s.d. values (0.040 °C s.d.$^{-1}$), indicating statistical significance above the 95% confidence level (Fig. 2b). We also use this bootstrap test to check the NPMM forcing on ENSO (Fig. 3 and Supplementary Fig. 4), the enhanced western Pacific zonal wind response (Fig. 4d and Supplementary Fig. 8) and the model experiment results (Fig. 5c–f).

**E-index and C-index.** A C-index and an E-index are used to determine extreme ENSO events in models[51]. We apply an empirical orthogonal function (EOF) analysis to the quadratically detrended D0JF1 SST anomalies of tropical Pacific (15° S–15° N, 140° E–80° W) over 1900–2099. The leading two principal components (PC1 and PC2) of the EOF analysis that correspond to a respective positive phase of EOF1 (warm anomaly centre in the central eastern Pacific) and EOF2 (a warm anomaly centre in the central Pacific and a cool anomaly aside) are both scaled to have an s.d. of 1. The C-index and E-index are then defined by [(PC1 + PC2)/2] and [(PC1 − PC2)/2], respectively.

**WESp and decomposition.** The WESp is estimated by a change in latent heat flux per unit change in zonal wind speed[5,41–43]. By substituting a linearized standard bulk formula for the latent heat flux, the WESp can be calculated as:

$$\mathrm{WESp} = -\frac{\partial \mathrm{LH}}{\partial u} = -\mathrm{LH}\frac{u}{W^2} \tag{1}$$

where LH is latent heat flux, $u$ is the 10 m zonal wind and $W$ is the total wind speed ($W$ in this work is directly obtained from model outputs). On the basis of the standard bulk formula, the LH can be decomposed into[52]:

$$\mathrm{LH} = L_v C_E \rho_a (q_s - q_a) W = L_v C_E \rho_a [q_s(T) - \mathrm{RH} \times q_s(T+S)] W \tag{2}$$

where $L_v$ is latent heat of evaporation, $C_E$ is the transfer coefficient, $\rho_a$ is surface air density, $S$ is air–sea surface temperature difference ($S = T_a - T$, $T_a$ is surface air temperature), $T$ is the SST and $q_s$ is saturation specific humidity. By integrating the Clausius–Clapeyron equation, the $q_s$ is analytically expressed by:

$$q_s(T) = \frac{\varepsilon e_0}{P} e^{-\alpha T_0} e^{\alpha T} = q_0 e^{\alpha T} \tag{3}$$

where $q_0$ is a constant ($2.862 \times 10^{-10}$ kg kg$^{-1}$), $\alpha = L_v/(R_v T^2) = \sim 0.06$ K$^{-1}$. Substituting equation (2) and equation (3) into equation (1), we obtain:

$$\begin{aligned} \mathrm{WESp} &= -L_v C_E \rho_a [q_s(T) - \mathrm{RH} \times q_s(T+S)] \frac{u}{W} \\ &= -L_v C_E \rho_a \left(1 - \mathrm{RH} \times e^{\alpha S}\right) q_s(T) u_W \\ &= -L_v C_E \rho_a q_0 \left(1 - \mathrm{RH} \times e^{\alpha S}\right) e^{\alpha T} u_W \end{aligned} \tag{4}$$

The variability of WESp is induced by variations of RH, $S$, $T$ and $u_W$. To estimate contributions of the individual term, we further decompose changes in the WESp into the following:

$$\Delta\mathrm{WESp} = \frac{\partial \mathrm{WESp}}{\partial\,(u_W)}\Delta\,(u_W) + \frac{\partial \mathrm{WESp}}{\partial \mathrm{RH}}\Delta\mathrm{RH} + \frac{\partial \mathrm{WESp}}{\partial T}\Delta T + \frac{\partial \mathrm{WESp}}{\partial S}\Delta S + R \tag{5}$$

$$\frac{\partial \mathrm{WESp}}{\partial\,(u_W)}\Delta\,(u_W) = \left[-L_\mathrm{v}C_\mathrm{E}\rho_\mathrm{a}q_0 \times e^{\alpha T}\left(1-\mathrm{RH}\times e^{\alpha S}\right)\right]_\mathrm{PD}\Delta\,(u_W) \tag{6}$$

$$\frac{\partial \mathrm{WESp}}{\partial \mathrm{RH}}\Delta\mathrm{RH} = \left[L_\mathrm{v}C_\mathrm{E}\rho_\mathrm{a}q_0 \times e^{\alpha(T+S)} \times u_W\right]_\mathrm{PD}\Delta\mathrm{RH} \tag{7}$$

$$\frac{\partial \mathrm{WESp}}{\partial T}\Delta T = \left[-\alpha L_\mathrm{v}C_\mathrm{E}\rho_\mathrm{a}q_0 \times \left(1-\mathrm{RH}\times e^{\alpha S}\right) \times e^{\alpha T} \times u_W\right]_\mathrm{PD}\Delta T \tag{8}$$

$$\frac{\partial \mathrm{WESp}}{\partial S}\Delta S = \left[\alpha L_\mathrm{v}C_\mathrm{E}\rho_\mathrm{a}q_0\mathrm{RH} \times e^{\alpha(T+S)} \times u_W\right]_\mathrm{PD}\Delta S \tag{9}$$

where PD and Δ denote mean value in the present-day climate (1900–1999) and changes in the mean value between future (2000–2099) and present-day climates, respectively. Equations (6–9) indicate changes in the WESp because of changes in wind speed (equation (6)), relative humidity (equation (7)), SST (equation (8)) and air–sea surface temperature difference (equation (9)). The total wind speed can be decomposed as:

$$W = \sqrt{u^2 + v^2 + w_*^2} \tag{10}$$

where $w_*$ is turbulent background wind speed[9]. Since zonal wind dominates the WES feedback, equation (6) can be simply expressed by (see also ref. [26]):

$$\frac{\partial \mathrm{WESp}}{\partial\,(u_W)}\Delta\,(u_W) \sim \Delta\,(u_W) = \Delta\left(\frac{u}{\sqrt{u^2+v^2+w_*^2}}\right) \sim \Delta\left(\frac{1}{\sqrt{1+\left(\frac{w_*}{u}\right)^2}}\right) \tag{11}$$

Equation (11) indicates that a stronger mean zonal wind corresponds to a more intense WES feedback, and vice versa.

**Intermediate model description.** The intermediate climate model used in this study consists of a Community Atmosphere Model version 3.1 (CAM3.1) and a Zebiak–Cane type 1.5-layer reduced-gravity ocean model[53,54]. The atmospheric and oceanic components are fully coupled with flux corrections (CAM3.1-RGO model hereafter)[55,56]. The CAM3.1 has a T42 horizontal resolution and 26 vertical levels, while the RGO has a 1° latitude by 2° longitude resolution covering a global domain (see ref. [55] for details of this model). The CAM3.1-RGO model has been frequently used to study NPMM or climate change-related questions[4,11,45] as the effects of different dynamic processes are easier to decipher in this model than in the CGCMs.

**Single-model ensemble experiments.** We conduct a 500 yr control run (CTRL) and a 400 yr quadrupled $CO_2$ concentration run ($4\times CO_2$) using CAM3.1-RGO. The CTRL is forced by the observed atmospheric composition in 1990 (constant $CO_2$ concentration of 355 ppm) and the $4\times CO_2$ starts from the hundredth year of CTRL with a sudden quadrupling (1,420 ppm) of $CO_2$ concentration. On the basis of the respective equilibrium state of CTRL and $4\times CO_2$ with slightly different initial conditions, two sets of 30-member initial-value ensemble runs are carried out. For each member, we initiate the observed positive NPMM SST pattern (Supplementary Fig. 1a) amplified by a factor of 4 (to increase a response signal) over the subtropical Pacific on the first day of March. The imposed anomaly is enough for our intermediate climate model to have an NPMM signal through March to May that is comparable to the observed. The model is then free to run for one year within the fully coupled framework. In addition, two parallel sets of 30-member ensemble experiments with zero SST anomalies initiated are performed. All the ensembles are initialized on 1 March when the NPMM forcing is applied. The oceanic and atmospheric responses to the imposed NPMM SST forcing are obtained by the differences between the corresponding experiments with and without initiated NPMM SST anomalies. The experiments reflect changes in the impact of NPMM on the tropical Pacific from CTRL (resembling historical simulations of CMIP5/6) to $4\times CO_2$ condition (resembling RCP8.5/SSP585 simulations of CMIP5/6). Similar initial-value ensemble experiments using the CAM3.1-RGO model were performed to study tropical inter-basin interactions[45].

## Data availability

Data related to the paper can be downloaded from the following websites: HadISST v1.1, https://www.metoffice.gov.uk/hadobs/hadisst/; NCEP/NCAR Reanalysis, https://www.esrl.noaa.gov/psd/data/gridded/data.ncep.reanalysis.derived.html; CMIP5 database, https://esgf-node.llnl.gov/projects/cmip5/; CMIP6 database, https://esgf-node.llnl.gov/projects/cmip6/. A detailed reference and DOI for each CMIP6 model are provided in the Supplementary Information. The CAM3.1-RGO model experiment data are available from the corresponding authors on request.

## Code availability

Codes for calculating MCA and NPMM pattern are publicly available via Zenodo at https://doi.org/10.5281/zenodo.5147938 (ref. [57]). All other codes are available from the corresponding author on request.

## References


46. Rayner, N. A. et al. Global analyses of sea surface temperature, sea ice, and night marine air temperature since the late nineteenth century. *J. Geophys. Res.* **108**, 4407 (2003).
47. Kalnay, E. et al. The NCEP/NCAR 40-year reanalysis project. *Bull. Am. Meteorol. Soc.* **77**, 437–471 (1996).
48. Taylor, K. E., Stouffer, R. J. & Meehl, G. A. An overview of CMIP5 and the experiment design. *Bull. Am. Meteorol. Soc.* **93**, 485–498 (2012).
49. Eyring, V. et al. Overview of the Coupled Model Intercomparison Project Phase 6 (CMIP6) experimental design and organization. *Geosci. Model Dev.* **9**, 1937–1958 (2016).
50. Austin, P. C. & Tu, J. V. Bootstrap methods for developing predictive models. *Am. Stat.* **58**, 131–137 (2004).
51. Takahashi, K. & Dewitte, B. Strong and moderate nonlinear El Niño regimes. *Clim. Dyn.* **46**, 1627–1645 (2016).
52. Richter, I. & Xie, S.-P. The muted precipitation increase in global warming simulations: a surface evaporation perspective. *J. Geophys. Res.* **113**, D24118 (2008).
53. Zebiak, S. E. & Cane, M. A. A model El Niño–Southern Oscillation. *Mon. Weather Rev.* **115**, 2262–2278 (1987).
54. Clement, A. C., Seager, R., Cane, M. A. & Zebiak, S. E. An ocean dynamical thermostat. *J. Clim.* **9**, 2190–2196 (1996).
55. Fang, Y. *A Coupled Model Study of the Remote Influence of ENSO on Tropical Atlantic SST Variability*. PhD thesis, Texas A&M Univ. (2005).
56. Chiang, J. C. H., Fang, Y. & Chang, P. Interhemispheric thermal gradient and tropical Pacific climate. *Geophys. Res. Lett.* **35**, L14704 (2008).
57. Jia, F. Code for MCA and regression. *Zenodo* https://doi.org/10.5281/zenodo.5147938 (2021).


## Acknowledgements


This work is supported by the Strategic Priority Research Program of Chinese Academy of Sciences, grant number XDB40030000. F.J. is supported by the National Key Research and Development Program of China (2020YFA0608801), National Natural Science Foundation of China (NSFC) projects (41876008, 41730534) and Youth Innovation Promotion Association of Chinese Academy of Sciences (2021205). B.G. is supported by NSFC projects (41922039, 91858102) and National Key Research and Development Program of China (2019YFA0607001, 2016YFA0601804). W.C. is also supported by CSHOR. CSHOR is a joint research Centre for Southern Hemisphere Oceans Research between QNLM and CSIRO. The funders had no role in study design, data collection and analysis, decision to publish or preparation of the manuscript. We acknowledge the World Climate Research Programme, which, through its Working Group on Coupled Modelling, coordinated and promoted CMIP6. We thank the climate modelling groups for producing and making available their model output, the Earth System Grid Federation (ESGF) for archiving the data and providing access, and the multiple funding agencies who support CMIP6 and ESGF.


## Author contributions

F.J., W.C. and L.W. designed the research; F.J. performed the experiment, analysed the data and wrote the initial manuscript with W.C.; B.G. contributed to the mechanism analysis; all authors contributed to interpreting results and improving this paper.

## Competing interests

The authors declare no competing interests.

## Additional information

**Supplementary information** The online version contains supplementary material available at https://doi.org/10.1038/s41558-021-01139-x.


**Correspondence and requests for materials** should be addressed to Wenju Cai or Lixin Wu.


**Peer review information** *Nature Climate Change* thanks Jing Ma and the other, anonymous, reviewer(s) for their contribution to the peer review of this work.